Received: 11 November 2021 | Revised: 10 March 2022 | Accepted: 28 May 2022

DOI: 10.1002/rob.22102

RESEARCH ARTICLE

WILEY

An autonomous robot for shell and tube heat exchanger inspection

Bujingda Zheng[1] | Jheng-Wun Su[2] | Yunchao Xie[1] | Jonathan Miles[1] | Hong Wang[1] | Wenxin Gao[1] | Ming Xin[1] | Jian Lin[1,3]

[1]Department of Mechanical and Aerospace Engineering, University of Missouri, Columbia, Missouri, USA

[2]Department of Physics and Engineering, Slippery Rock University, Slippery Rock, Pennsylvania, USA

[3]Department of Electrical Engineering and Computer Science, University of Missouri, Columbia, Missouri, USA

Correspondence
Jian Lin, Department of Mechanical and Aerospace Engineering, University of Missouri, Columbia, MO 65211, USA.
Email: linjian@missouri.edu

Funding information
U.S. Department of Energy

Abstract

Shell and tube heat exchangers (STHEs) are critical to energy conversion efficiency of power plants. Eddy current examination is a way to evaluate working conditions of these tubes. However, the current testing apparatus requires human to manually insert an eddy current testing (ECT) probe into and extract it out of individual tubes, and meanwhile monitor measurement results for diagnosis. It is a time-consuming and labor-intensive procedure even for an experienced technician. To tackle this challenge, in this study, we developed a robot enabled ECT system for autonomous inspection of STHEs. The robotic platform employs Mecanum wheeled chassis for high mobility, machine vision to locate tube bundle and tube inlets, a rotational Cartesian mechanism to operate at planes with all possible inclinations, and a task-specific mechanism for ECT probe delivery. Machine vision locates tube bundle and tube inlets by an April tag detection algorithm and a Circle Hough Transform algorithm, respectively. Assisted by a guiding cone, the ECT probe is continuously fed into the tubes with a fill factor of 0.819. During this process, the eddy current data are automatically collected and real-time analyzed by convolutional neural networks, showing accuracy of nearly 100% for identifying defective and nondefective tubes and 85% for four types of defective tubes and nondefective tubes.

KEYWORDS
autonomy, deep learning, eddy current testing, heat exchanger, robot

1 | INTRODUCTION

By 2050, there will be a 30% increase in global energy consumption. Energy generation in the form of electricity is expected to be doubled. Although clean and renewable energy has an increasing share (Gritsevskyi, 2016; Melani et al., 2019), in the next few decades at least, electricity generated by burning fossil fuels in power plants will still be dominant in modern society (Richardson, 2014; Speight, 2021). Making power plants highly efficient is still imperative. Regular maintenance of key components such as heat exchangers for energy transfer between liquid of different temperatures is essential to this goal since the energy conversion efficiency is greatly affected if they are subjected to structural discontinuities, such as pitting, cracking and wall loss (Richardson, 2014; Speight, 2021). Eddy current testing (ECT) is a mainstream nondestructive examination (NDE) technique to inspect the heat exchanger tube (Sadek, 2006). Visual examination can identify large defects (Hayashi et al., 2014; Xiong et al., 2019; Yamamoto et al., 2014), while ECT based NDE is more suitable for small internal or exterior defects (García-Martín et al., 2011).

Among various types of heat exchangers used in the power plants, shell and tube heat exchangers (STHEs) are the most common one with 65% market share globally (Smith, 2005). They are usually arranged in a parallel and closely packed form (Figure 1a). Insertion and extraction of an ECT probe into and out of these individual tubes

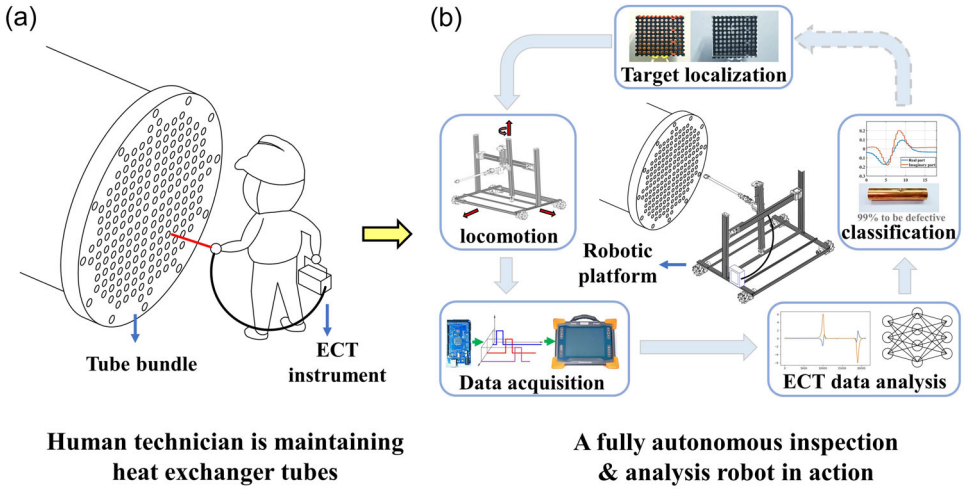

FIGURE 1 Schematic showing a human worker performing shell and tube heat exchanger inspection using ECT. ECT, eddy current testing.

and meanwhile monitoring measurement results for real-time decision making is a time-consuming and labor-intensive procedure even for an experienced technician. In addition, high reliance on human workers to manipulate the inspecting instrument may enlarge the operational inconsistency, which may lead to false diagnosis due to increased variance of collected ECT data (Udpa et al., 2004). Not only this restricts the efficiency of maintenance, but also limits the detection accuracy (Sadek, 2006). Therefore, it is imperative to come up with a solution that minimizes variance in both instrument manipulation and data analysis.

In this article, we present a robot-enabled ECT system for autonomous inspection of STHEs (Figure 1b). The robot uses machine vision to perceive the surroundings and locate the working area. Different mechanisms were developed for different types of tasks. Mecanum wheel chassis was designed for high mobility. A Cartesian mechanism with close-loop linear actuators was employed for precise motion. To real-time perform ECT data analysis and decision making, deep learning models were developed. Main contributions of this study include: (1) a cost-effective autonomous robotic platform with seven degrees of freedom (DOF) for autonomous testing of STHEs; (2) development of accurate deep learning models for ECT data analysis based on limited data.

2 | RELATED WORKS

Robots have been widely used in modern industries for various applications. They are well suited for repetitive tasks, such as welding, assembling, and inspection. They are capable of working in environments that are not friendly to humans (Djuric et al., 2016). Additionally, robots yield low and constant operational errors (Engelberger, 2012). The development of robots for the pipe inspection has been reported. For the pipes made of ferromagnetic materials, Schoeneich et al. developed robots with magnetic wheels to make them stay on the pipe wall (Schoeneich et al., 2010). They can perform visual inspection along ferromagnetic tubes with diameters of ≥25 mm. Due to the train-like design, the robots can pass the curved pipes with a maximum curvature of 150 mm. But occurrence of slippage fails to match displacement of the robots with the sensed one. Fischer et al. demonstrated magneBike for inspecting ferromagnetic components, which can deal with convex edges and climb vertical wall (Fischer et al., 2009). For the pipes made of nonferromagnetic materials, the robots adopt actuation wheels to apply pressure to the wall through a compliant mechanism for locomotion (Chang et al., 2015; Kwon & Yi, 2012; Kwon et al., 2010; Qu et al., 2018). Nevertheless, these robots are limited to function inside relatively large tubes and are powerless when dealing with parallelly and closely packed STHEs. Furthermore, they mainly examine the pipes through visual sensors and hence would omit invisible defects.

Some companies, such as Waygate, developed robots that can clean outer surface of boiler wall and detect flaws by an ultrasound sensor. Westinghouse corporation launched a task-specific robot, Pegasys, for STHEs inspection. It can walk on the cross-section of the STHE bundles through pneumatic grippers and is capable of delivering the testing probes into individual tubes. B&W NE/Intech developed their Spyder serial robots for steam generator inspection. A PRIMA system from BWX Technologies is a manipulator designed to operate multiple modular tools for tube inspection. However, all these commercial robots need to be installed at the working area in advance and have no capability of analyzing data for real-time decision making. Therefore, an integrated robotic system that can autonomously deploy probing sensors into pipes with various dimensions, actuate high precision travelling displacement, and real-time process acquired data for STHE inspection is highly desired.

For ECT data analysis, many researchers have recently used deep learning methods. Miao et al. demonstrated a convolutional neural network (CNN) to identify defects of narrow lap welds. The accuracy

was reported to be 96.94% for five classes (Miao et al., 2019). Deng et al. applied a CNN model to analyze image ECT data of titanium plates with defects of different geometries. It delivered a classification accuracy of 95.68% even with the presence of noise (Deng et al., 2020). However, significant amount of data was needed for the model training. As it is costly to obtain ECT data from objects with varied materials and dimensions, it is hence necessary to develop a new method that can be trained using much less data and show better robustness. In the realm of image analysis, researchers improved the generalization and robustness of models through data augmentation methods, such as adjusting brightness, random erasing, rotation, and so on (Park et al., 2019; Shorten & Khoshgoftaar, 2019).

3 | SYSTEM DESIGN AND CONSTRUCTION

The proposed autonomous robot should be able to perform three tasks. The first one is to locate the tube bundle and determine tube inlet position. The second one is to actuate motion toward target followed by precisely manipulating the ECT probe into the STHEs. Finally, it should be able to determine the tube status by performing real-time data analysis. To realize these tasks, environmental perception unit, mechanical actuators, control system, and deep learning model were developed and integrated.

3.1 | Mechanical system design and construction

The mechanical system consists of a chassis of high-mobility and rotational Cartesian mechanism (Figure 2a). The chassis is controlled by an Arduino Mega 2560 and the rotational Cartesian mechanism receives command from MKS GEN V1.4 microcontroller. The electronic components of the system are described in Figure 2b. The constructed robot has seven DOF as illustrated in Figure 2c. Three DOFs are attributed to the chassis using four Ilon's Mecanum wheels (Ilon, 1975) for locomotion, whose control algorithm was developed based on the kinematic model developed by Taheri et al. (2015). The remaining four DOFs are attributed to the rotational Cartesian mechanism, which uses a rotation actuator to adjust the inclination of a dual-direction dual-rail linear system that holds cameras, the ECT probe, and the probe delivery system. The rotation actuator with chassis can coaxially align the ECT probe with the tube inlets.

One of the design goals of the system is to deliver the ECT probe into the tubes at a constant feed rate. To achieve this goal, a mechanism similar to the FDM 3D printer filament delivery system was initially tried. It clamps the probe through a passive groove wheel and an actuation gear. The passive wheel was placed on a tensioning lever to induce enough friction between the probe cable and the actuation gear (Figure 2c-v, Figure 3a). However, the probe cable was still too slippery during the movement. Occurrence of slippage resulted in discontinuous probe delivery. To solve this issue, a rack and pinion typed delivery mechanism was eventually developed. Three racks, each of which has three gears, are arranged as 120 degrees apart and are tightly wrapped around the probe cable. The active gear on the top drives motion of the cable while the two passive ones help to hold the probe cable. The rack is 170 mm in length and longer than the test tube with a length of 90 mm (Figure 3b,c). This system can deliver the probe at a speed of 20 mm/s without slippage so that locations of defects in the tube detected from the abnormal signal from the collected ECT data can be precisely identified. A guiding cone was installed in the front of the probe to improve the insertion success rate. Demonstration of the rotational Cartesian mechanism and probe delivery system is shown in Video S1.

3.2 | ECT data acquisition unit

A Reddy AC & Tubing ECT unit (Eddify Technologies) and a bobbin probe made by Eddyfi company were used to acquire the ECT data (Figure S1a,b). With a microcontroller sending transistor-to-transistor logic (TTL) signals to this instrument through different I/O pins (Figure S1), the instrument can perform a data acquisition task automatically. The corresponding TTL signals trigger actions of start acquisition, stop acquisition, and data saving. The data are automatically saved and wirelessly transmitted to an onboard PC through a local WIFI network. Then they are input into a pre-trained deep learning model for classification. Demonstration of probe delivery and data acquisition subsystems is shown in Video S2.

3.3 | Machine vision

In robotic research, some tasks cannot be fulfilled without acquiring positions and orientations of a certain object. For many target acquisition systems (Arad et al., 2020; Birrell et al., 2020; Williams et al., 2020; Xiong et al., 2020), their end effectors must be aligned with the target through a vision-based approach. However, they do not require detection and control of the relative orientations between the target and the end effectors. In contrast, in our mobile robotic platform, to achieve successful probe insertion into the tube inlets, the relative orientations of the tube bundle plane to the probe must be accurately detected and controlled. The plane orientation estimation can be done with assistance of a stereo camera (Se & Brady, 2002). By an image processing algorithm, the obtained 2D images can be used to construct 3D depth images to estimate the ground planes (Cherian et al., 2009). In our work, two machine vision cameras were integrated into the system. The first one is the OpenMV camera, which has two functions: object detection of tube bundles and estimation of plane orientations. For testing purposes, a tube bundle mockup made of 90 tubes was used (Figure 4a). These copper tubes (from Mcmaster–Carr) with a length of 90 mm, outer and inner diameters of 19.05 and 16.57 mm were mounted onto a perforated plate with a dimension of 315 mm × 286 mm. The tube dimension, spacing, and a pitch ratio of 1.43 were all selected based on an STHE design standard (T.E.M. Association, 1952).

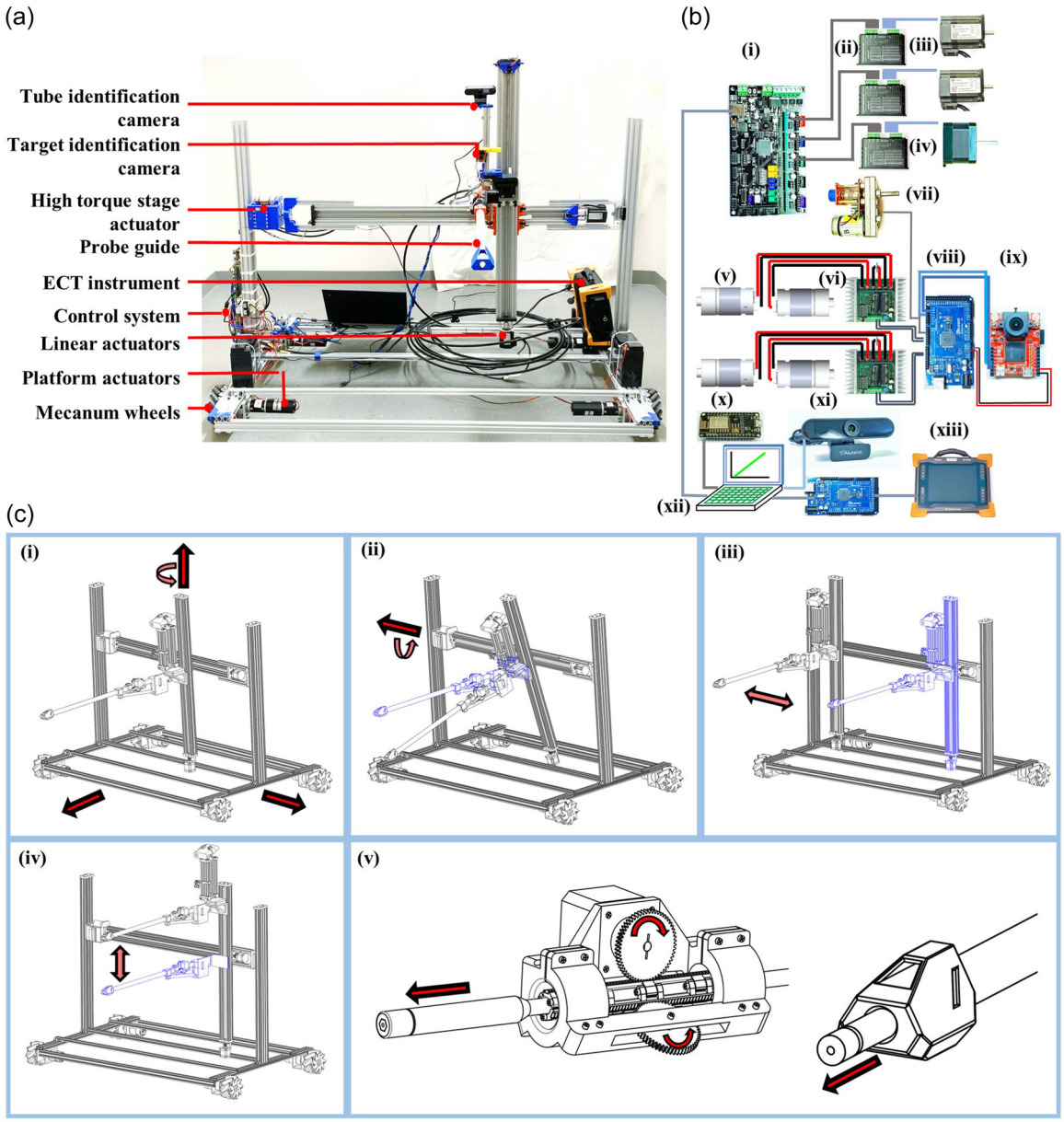

FIGURE 2 System layout and distribution of seven DOFs. (a) A prototype of a fabricated autonomous robotic platform. (b) Photographs of key electronic components: (b-i) MKS gen V1.4 controller; (b-ii) DM542T stepper motor driver; (b-iii) a Leadshine CS-M22313 stepper motor; (b-iv) NEMA 17 stepper motor; (b-v) a DC motor; (b-vi) Saber tooth DC motor driver; (b-vii) ASME-MXB high torque servo motor; (b-viii) Arduino Mega 2560; (b-ix) OpenMV H7; (b-x) ESP8266; (b-xi) HD camera; (b-xii) onboard PC; (b-xiii) Reddy AC and Tubing ECT instrument. (c) (c-i) Three DOFs from chassis locomotion; (c-ii) One DOF from rotational motion of the rotational Cartesian mechanism; (c-iii, c-iv) Two DOFs from the linear motion of the rotational Cartesian mechanism; (c-v) 1 DOF from a probe delivery system. DOF, degree of freedom.

By Equation (1), the fill factor of the current setting is 0.819. Then they are input into a pre-trained deep learning model for classification. Demonstration of probe delivery and data acquisition subsystems is shown in Video S2.

$$\eta = \left(\frac{D_0}{D_i}\right)^2, \tag{1}$$

where η is the fill factor, D_0 is the outer diameter of probe, and D_i is the inner diameter of tube.

To assist the object detection and plane estimation, a tube-bundle-fixed fiducial marker, called an April Tag, was attached to the plate of the tube bundle mockup (Figure 4b). First, the OpenMV camera can locate the tube bundle by identifying the fiducial marker (Olson, 2011; J. Wang & Olson, 2016). Then the camera performs the second function: estimation of the plane orientations. The purpose of doing the plane orientation estimation is to ensure that the ECT probe is well aligned with the tubes for smooth delivery. Based on the position and orientation of the fiducial maker in the image, the camera can return two translational and two orientational positions of the maker-attached tube bundle.

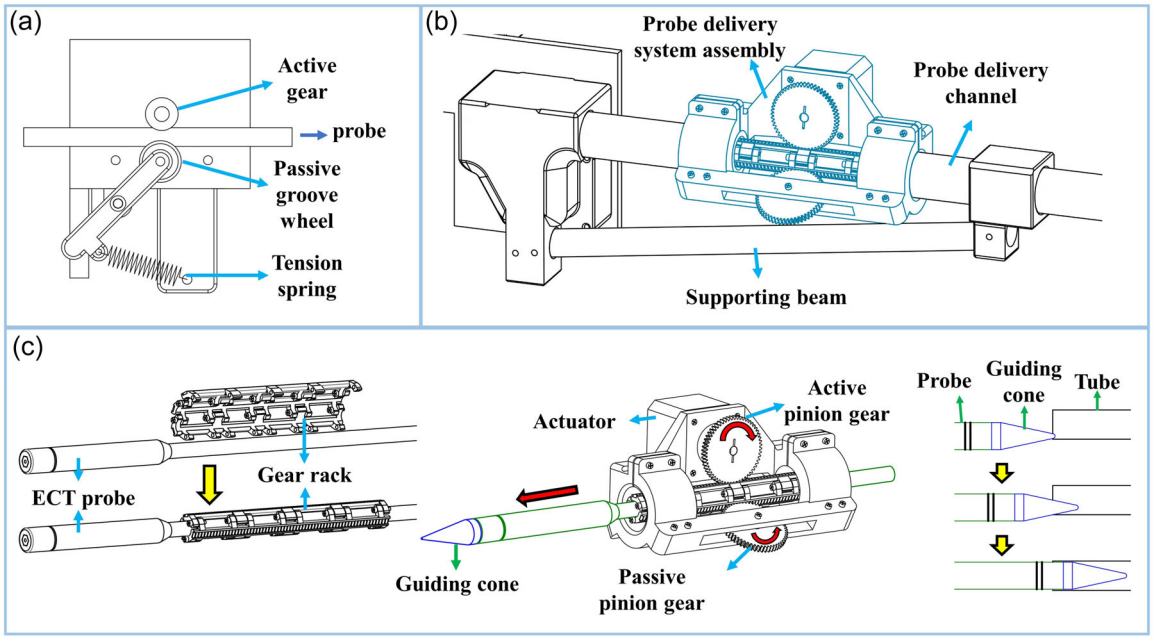

FIGURE 3 A probe delivery system. (a) CAD drawing of an initial design of a probe delivery mechanism. (b) CAD drawing of improved design of a probe delivery system. (c) CAD drawing of rack assembly and schematic showing probe delivery principle. CAD, computer-aided design.

A fiducial marker in the center of the image without distortion will yield zero translation and orientation (Olson, 2011; J. Wang & Olson, 2016). Δx and Δy are translational displacements along the x and y axes, respectively, while α and β are the orientational angles about the z and y axes, respectively (Figure 4c). Δx and Δy are used to align the chassis of the robot to the tube bundle, while α and β are used to estimate the relative angles of the ECT probe to the plate where the tubes are held. These four parameters are dynamically collected and fed to four respective PID controllers as the input to control the actuators to reposition the robot. The goal of the control is to make Δx, Δy, α and β zero. As a result, the fiducial marker in the center of the image should not be distorted. Note that, the four parameters Δx, Δy, α, and β are sufficient for the robot to coaxially align the delivery probe with the tube inlets.

The performance of the four PID controllers was tested. Figure 4d shows the response curves of Δx, Δy, α and β. They show that within a few seconds the PID controllers actuate the robot to the target position, although there exist some lags for Δx, Δy and α, which may be due to relative sliding between test ground and Mecanum wheels. This hypothesis is validated by the performance of the controller that controls a rotation actuator to adjust β, which shows much less lag. These results indicate the feasibility of using a fiducial marker to obtain the four repositioning parameters for navigating and aligning the robot. Fiducial marker-assisted robot navigation is demonstrated in Video S3.

The second machine vision camera is an Aluratek 1080 HD camera, which was used to acquire the center point coordinates of the individual tube inlets. It was placed above the probe delivery channel with an installation angle of 19° for better target capturing (Figure 5a). Due to this installation angle, the tube bundle image is distorted if not corrected. As a result, the image would not show equally spaced tube inlet center coordinates as they are supposed to be. To solve this issue, perspective transformation was applied to the raw image for correction until the circle detection algorithm can feedback circle center coordinates that were equally spaced in both horizontal and vertical directions (Figure 5b). After image correction, a Circle Hough Transformation (CHT) algorithm for detecting circles was employed to rapidly obtain the tube inlet center coordinates of the individual tube inlet. In the CHT algorithm, Equation (2) was used to describe the circle in the original image space, the circle has a center (a, b) and radius r. As tubes used for simulation are of the same dimension, the radius is therefore a constant.

$$(x_i - a)^2 + (y_i - b)^2 = r^2 \tag{2}$$

Each point on the circle edge in image space corresponds to a circle of center (x_i, y_i) and radius r in the parameter space. These circles can be expressed by Equation (3). If a circle in the image space is correctly detected, corresponding circles in the parameter space will intersect at a certain (a, b).

$$(a - x_i)^2 + (b - y_i)^2 = r^2. \tag{3}$$

The accumulator matrix used for tracking intersection points can be written as $A(a, b)$, which contains all points of circle edge in the parameter space. If an intersection is detected at (a, b), the element $A(a, b)$ will be added by 1, Equation (4). In this way, the point (a, b) where most circles intersect will have the highest vote. The local maximum leads to the center of the detected circle.

$$A(a, b) = A(a, b) + 1. \tag{4}$$

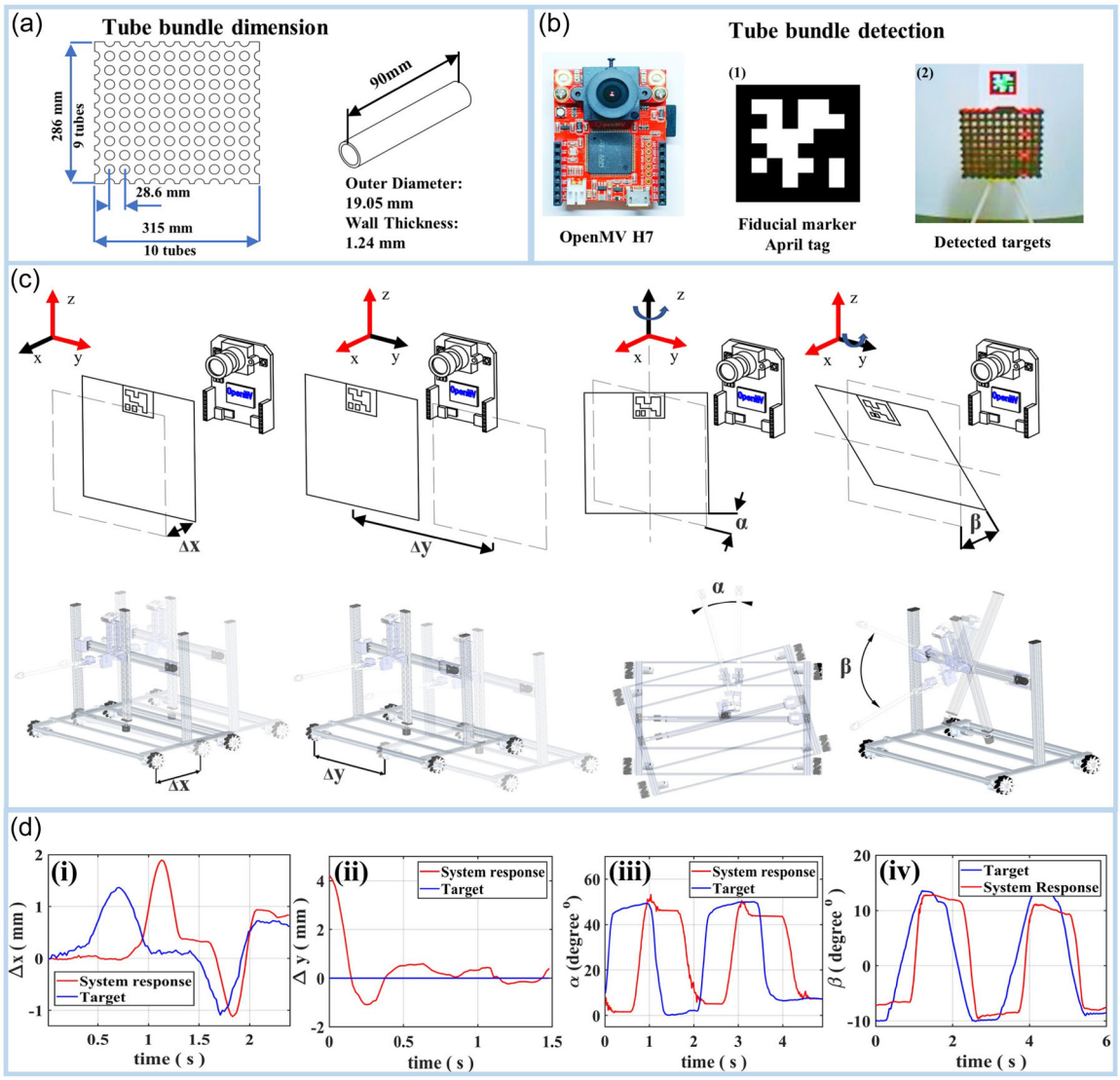

FIGURE 4 (a) A schematic showing a tube bundle mockup and the tube arrangement. (b) An OpenMV camera used to detect the tube bundle, a fiducial marker, and detection result. (c) Schematic showing Δx, Δ*y*, *α* and *β* as well as the principle of obtaining them by machine vision. (d) Response curves of (d-i) Δ*x*, (d-ii) Δ*y*, (d-iii) *α*, and (d-iv) *β* controllers.

Correction and detection of a sample perforated plate and tube bundle mockup are illustrated in Figure 5b-c. The raw input was first undistorted by perspective transformation (Figure 5b-ii), which is then followed by edge detection (Figure 5b-iii). The edge detection finds boundaries of objects in an image by a color gradient. Pixels on the boundary are then substituted into the CHT algorithm. Results of CHT over the testing plate are illustrated in Figure 5b-iv, where the intersections of red circles are the centers of circles. Figure 5c illustrates the application of perspective transformation and CHT in detecting the tube bundle mockup. Figure 5c-iii shows the center coordinates of circles in the image. The process of obtaining coordinates of the tube inlet centers is shown in Video S4. The OpenMV module communicates directly with Arduino Mega 2560 that controls the chassis and the rotation actuator of the Cartesian mechanism. With these obtained coordinates and angles of *α* and *β*, the Cartesian mechanism can align the probe to make the probe coaxial to the tubes for smooth insertion.

3.4 | Task sequence

The developed autonomous robot operates three sequential tasks of target localization and locomotion, ECT probe deployment, and data acquisition and analysis by three integrated sub-systems (Figure 6). First, machine vision (an OpenMV camera) can recognize the tube bundle and navigate the robot to the target until the target is in the center of the image and the distance threshold is met. By the method described in Section 3.3, Δ*x*, Δ*y*, *α* and *β* are estimated and serve as the input of the controller that actuates the chassis and rotational Cartesian mechanism to position the robot. The goal is to make all of them zero so that the probe is expected to be aligned coaxially with the tubes of interest.

After finishing the first task, the HD USB camera can identify the relative coordinates of individual tube inlets by the method as described in Section 3.3. The coordinates are then mapped and

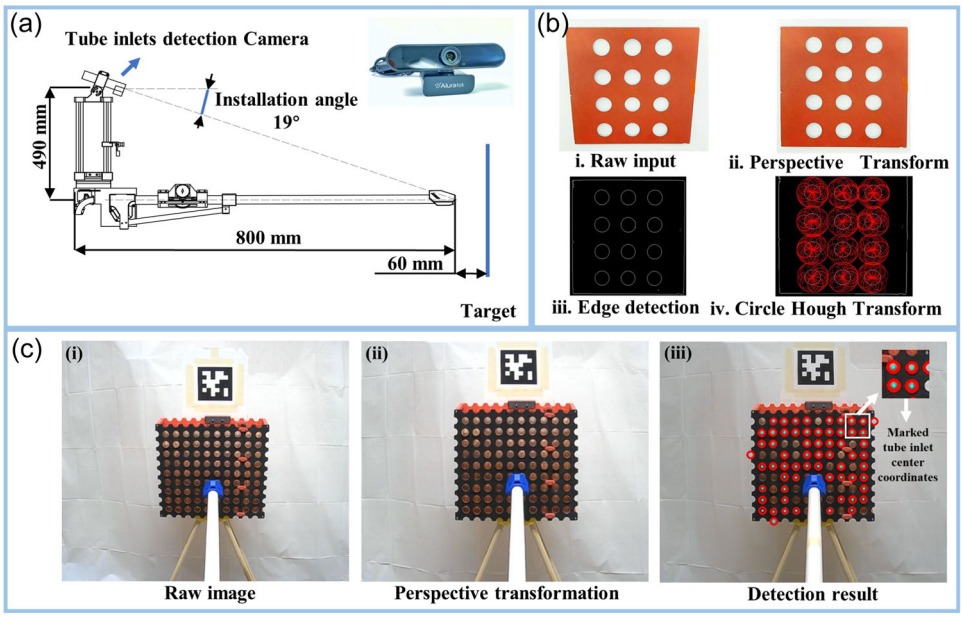

FIGURE 5 (a) A photograph of HD USB camera for acquiring the tube inlet coordinates and a scheme showing location of the camera and an installation angle. (b) Images before and after perspective transformation and images showing edge detection and Circle Hough transformation mechanism. (c) Images showing a correction process of obtaining coordinates of the tube inlet centers.

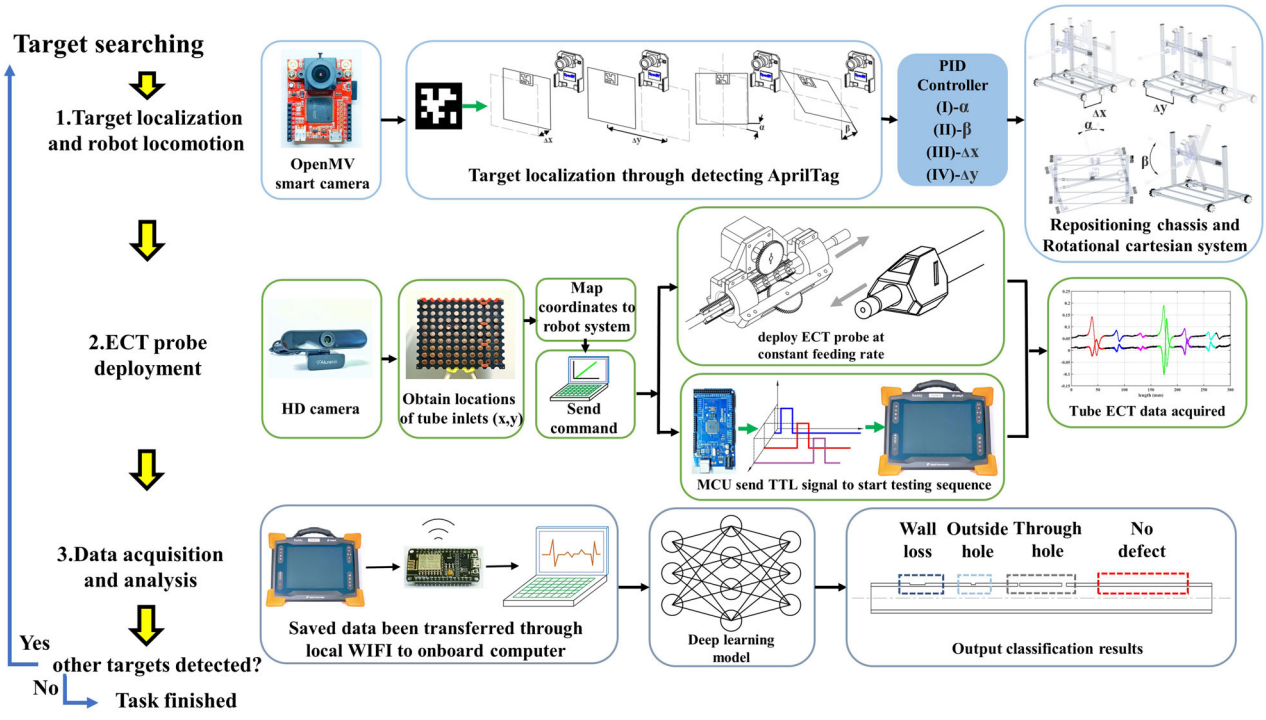

FIGURE 6 Workflow showing task sequence of the robot for autonomous shell and tube heat exchanger inspection.

served as the input of the controller that controls the motion of the ECT probe holder in the *y* and *z* axes (Videos S3 and S4). Accurate coordinates allow the probe to be inserted smoothly into tube inlets. During the probe delivery in Task 3, a TTL signal is sent to the ECT instrument to trigger start/stop data acquisition and data saving actions. Simultaneously, the collected ECT data are wirelessly sent to the onboard computer through local WIFI network for data analysis by a deep learning algorithm that can classify tube status.

This workflow to perform the three aforementioned tasks is repeated until all the tubes are detected. Demonstration of the whole task sequence in a simulated test environment is shown in Video S5.

4 | RESULTS AND DISCUSSION

4.1 | Positioning accuracy test

To evaluate the accuracy of the probe delivery mechanism, a simulated case was conducted. The probe was replaced by a laser pointer, which simulates the process of probe delivery by shooting the laser to the target as illustrated in Figure 7a. A simulated tube inlet with a diameter of 16.56 mm on a plate was placed in front of the robot. The robot first detected the inlet and then acquired the center coordinate of the inlet. Then the robot was navigated to the corresponding position and turned on the laser (Figure 7b). A camera placed behind the plate recorded the locations of the laser spot. Inspired by the probe and drogue method used in the in-flight refueling task (Bolien, 2018), which uses a funnel-shaped guiding basket to aid the docking process between the probe and hoses, we use a guiding cone to reduce the difficulty of probe insertion into the tube inlets. Its geometry is shown in Figure 7c. A successful insertion is guaranteed if the tip of the guiding cone lands inside the tube inlet as shown in Figure S2. Using Equation (S1), a tolerance region can be estimated as shown in Figure 7d. The test was repeated for 25 times. The testing results of the positioning accuracy for the tube inlet detection camera is shown in Figure 7e,f. Statistical analysis on the positioning data shown in Figure 7f shows that there is an average distance of 0.4147 mm and standard deviation of 0.2927 mm away from the center of the tubes. This positioning accuracy is high enough to actuate successful insertion of the probe into all the detected tubes, which are packed to form a plane with a dimension of 286 mm × 314.6 mm.

4.2 | A deep learning algorithm for ECT data analysis

To realize full autonomy, automatic analysis of the ECT data for detection of the tube defects is essential. To achieve the goal, a CNN was utilized in

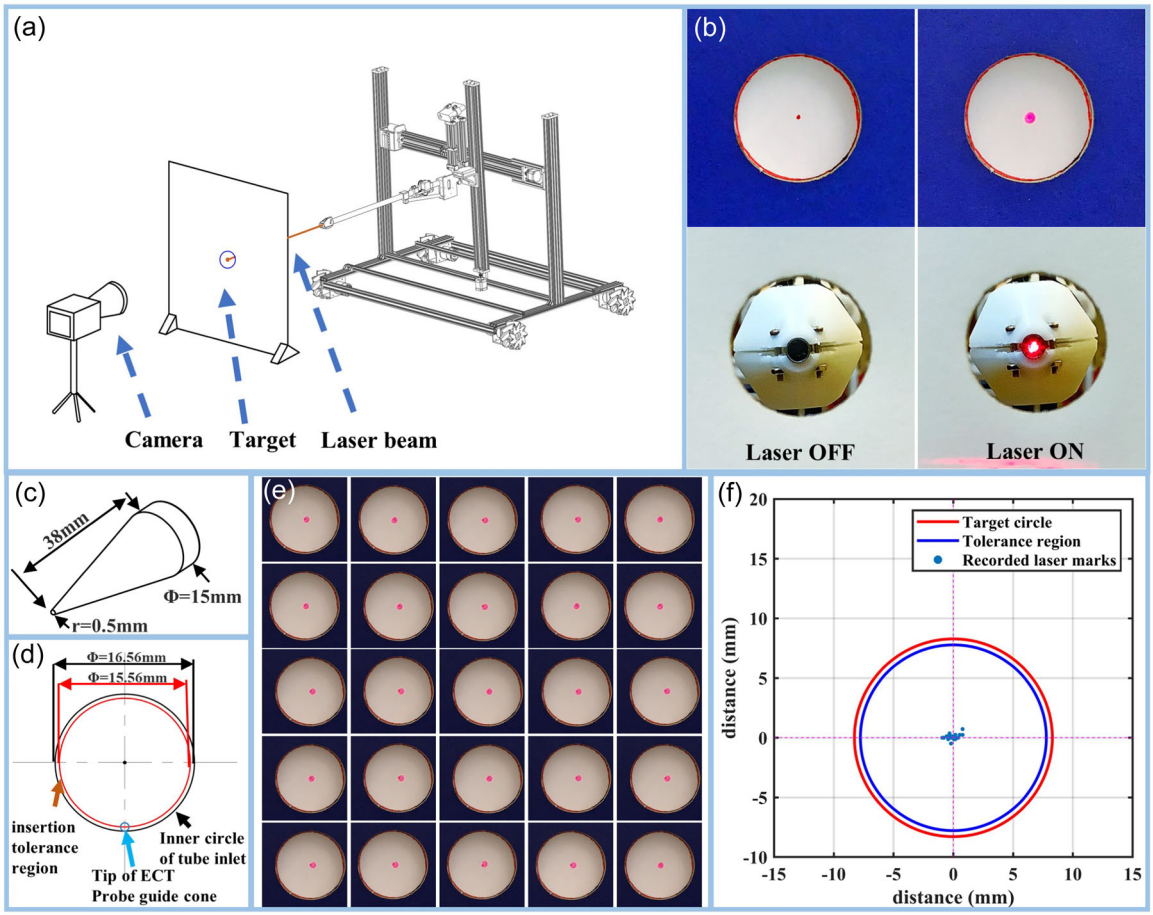

FIGURE 7 Evaluation of positioning accuracy of the Cartesian mechanism. (a) Schematic of an experiment setup for accuracy evaluation. (b) Images of laser spots when the laser is switched off and on. (c) Geometry of a probe guide cone placed in front of the eddy current testing probe. (d) Schematic showing tolerance of successful probe insertion. (e) Locations of 25 repeated laser spots in the tube inlet. (f) Distribution of the 25 laser spots in the tolerance region.

our system. To train the model, 10 high pressure copper tube sections for drinking water with four statuses were used for data collection. The four classes of status include no defect, wall-loss, through holes and outer holes of different sizes. These tubes and the corresponding ECT spectra of their defective areas are illustrated in Figure 8a. The blue and red lines are real and imaginary components of original ECT data, respectively. To obtain a robust deep learning model, ECT spectra data from different types of defective tubes are obtained. First, ECT data from 10 tubes

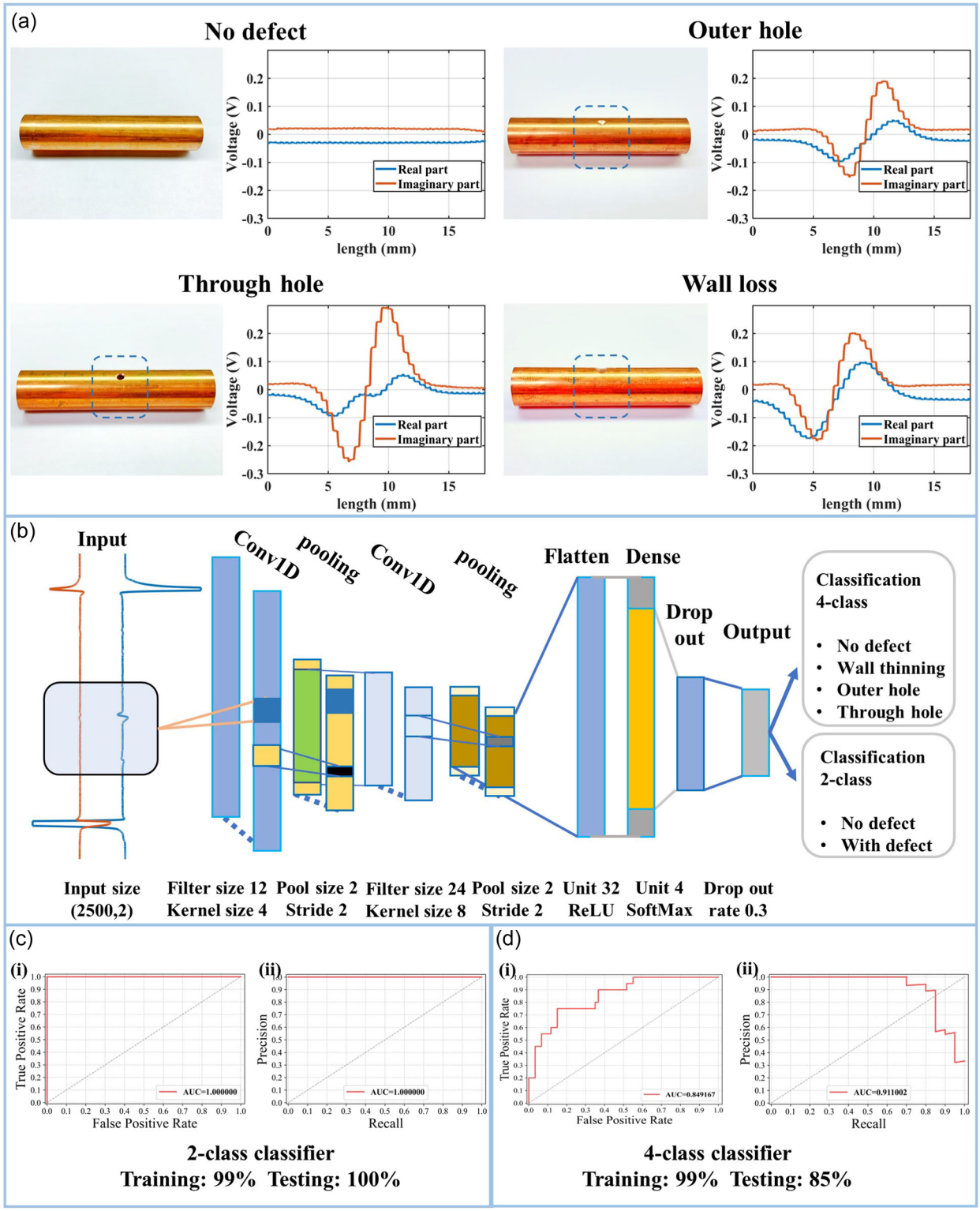

FIGURE 8 (a) Four types of tubes used for data collection and segmented eddy current testing spectra of defective areas. (b) CNN architecture and hyper parameters. (c) ROC and PR curves of a CNN model trained by data collected from nondefective and defective tubes. (d) ROC and PR curves of a CNN model trained by data from nondefective tubes and tubes with outer hole, through hole, and wall loss. CNN, convolutional neural network; PR, precision-recall; ROC, receiver operating characteristic.

showing four types of defective status (normal, outer hole, through hole, and wall loss) were collected and segmented. Second, four sets of segmented data were augmented through phase-shifting and noise addition as shown in our previously reported work (H. Wang et al., 2020). By these methods, these data were augmented to 40,000 spectra. Finally, 39,600 of them were used for model training and 400 of them were used for model validation. Meanwhile, additional 20 tubes with these four types of defective status were used for testing. The CNN architecture and hyperparameters of the finally trained model are illustrated in Figure 8b. Input of the model is the real and imaginary parts of the ECT data. Dimension of the input matrices is 2500 × 2. The data were first plugged into two sets of convolutional layer and max pooling layer for feature extraction, which is then followed by a flatten layer together with a dropout layer that keeps 70% of the data randomly. The flatten layer bridges the convolutional layers and a subsequent fully connected layer. The output of the CNN model is the probability of the four defect categories that best match the input data. After the successful training, our model showed a training accuracy of 99% and a testing accuracy of 85% for classifying these four categories. Recently, Zhu et al. reported a CNN model that classified only defective and nondefective two classes with accuracy of 99% from the ECT data (Zhu et al., 2019). Our model was trained with very limited data, while the model can classify four classes with a comparable accuracy. If the data were divided into two groups: defective and nondefective tubes, the trained model showed a testing accuracy of almost 100%.

Receiver operating characteristic (ROC) and precision-recall (PR) curves were employed as evaluation metrics of the model. ROC curve is an evaluation metric of classification problems under different thresholds. It illustrates the extent to which the model can distinguish between different categories. Deviation of the ROC curve from a random guess baseline to the upper left corner indicates that a machine learning model has achieved high prediction precision. AUC is the area under a ROC curve, which is equal to the probability that the classifier randomly ranks selected positive samples higher than randomly selected negative samples. Positive and negative samples are two types of data in binary classification. True positive rate and false positive rate are illustrated in Figure 8c–i, d-i. As the ROC curve is close to the upper left corner and AUC value equals to 1, it can be concluded that the model of binary classifier is more accurate than the quaternary classifier. The PR curve shows the ratio of the true positive number of correct predictions to the total positive number of predictions, which is presented in Figure 8c-ii, d-ii. Precision is the proportion between true positives and total positives. The recall rate measures whether the model can correctly identify true positives. It is desired to have a model that has both high precision and high recall. The precision value at recall of 1.0 is equal to 1, indicating high true positives from the binary classifier.

4.3 | Demonstration of autonomous operation

The fully integrated system was tested in a simulated environment. Demonstration of the autonomous process is shown in Video S5. In the test, tubes with defects (80 tubes) and without defects (20 tubes) were randomly mounted into a bundle. Figure 9a shows that the robot is delivering the ECT probe into a tube of interest. Use of a guiding cone enables smooth insertion. The probe delivery system also ensures continuous and constant delivery. Figure 9b-i shows a representative example tube that was detected to have a wall-loss defect after a successful probe delivery. After each probe deployment, the ECT data of the tube is first acquired and stored in the ECT instrument (Figure 9b-ii), and then is wirelessly transmitted to a computer for classification by the developed CNN models. In this process, the computer displays the status of data acquisition process, then the plot of raw ECT spectra. Simultaneously, the algorithm segments the data from the defective area into 2500 × 2 matrices, which are fed into the pre-trained CNN models for classification. In this example, both binary and quaternary classifiers show ~100% confidence in identifying it as a tube with wall-loss defect (Figure 9b-iii).

4.4 | Discussion

In this study, the robot meets the goal of autonomously inspecting STHEs. Compared with commercial robots, our robot requires less human intervention in terms of data analysis and decision-making. The robot can navigate itself in front of the tubes, and then coaxially align the probe delivery channel to the inlets of the tubes. Subsequently, the ECT probe was deployed along the tube for data collection while performing data analysis. Another contribution is that with the aid of data augmentation, we have developed a deep learning model with a high classification accuracy and high robustness. However, in other reported work, without using sufficient data, their models would suffer from the problems of overfitting or large variance. The success rate of inserting the probe into the tubes is mainly limited by positioning accuracy of the robot and tube inlet coordinate detection. The positioning and chassis locomotion are largely affected by the fiducial marker detection system. The resolution of the target detection camera, grip between Mecanum wheels and the ground, as well as stability of the rotation actuator, contribute to the positioning error of the robot. The maximum supported resolution of the tube bundle detection camera is 640 × 480. We used 160 × 120 to reduce the data collection load and accelerate the computation. Its detection accuracy is illustrated in Figure S3. Correspondingly, the mean absolute percentage error ranges from 1.49% to 34.22%. A servo motor with a higher torque for the rotation actuator can increase stability of the system. The accuracy of the tube inlet coordinate largely determines if the probe can be successfully inserted into a tube as it is only 1.57 mm larger than the probe outer diameter. This accuracy is affected by the light condition and camera resolution. A guide cone that is installed in the front of the probe can partially lower the system error. Without slippage, the rate of successful insertion into the detected tubes is 100%. The probe delivery speed into a tube with a length of 90 mm was set to 20 mm/s, leading to the execution time of 18 s per probe insertion.

Other improvements can be made to make the system more robust in future work. (1) One expected issue in the real field environment is the wheel slip. To increase the grip between the mobile platform and the ground, a tracked chassis can be used. (2) To

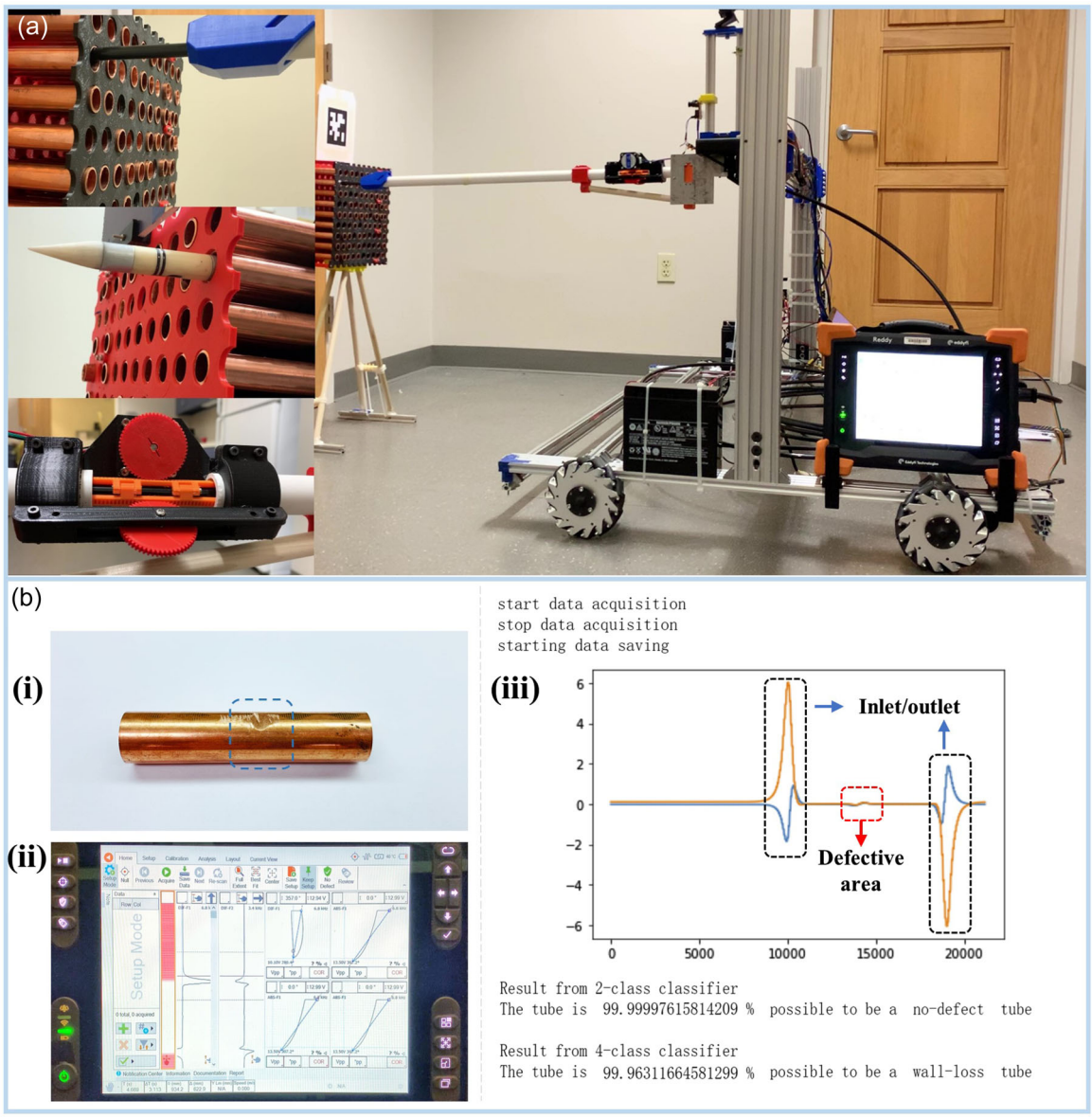

FIGURE 9 (a) A photograph showing that the robot is inserting ECT probe into a tube of interest. (b-i) A representative tube with a wall-loss defect. (b-ii) Snapshot displayed on the Reddy AC unit showing ECT spectra of the tube. (b-iii) An ECT spectrum of the whole tube including the defective area. The spectrum of the defective area was extracted as the input of the CNN model. Bottom panel shows the prediction output of the CNN model. CNN, convolutional neural network; ECT, eddy current testing.

deal with uneven ground and varying light conditions, active suspension with a light adaptive algorithm can be applied. Using a gimbal or multiple cameras with active light sources can provide a better field of view for out-of-sight marker detection. In addition, proximity sensor arrays can be added to empower the robot with a collision avoidance function. A strategy of detecting the tube inlets from multiple camera positions can be used to mitigate the issue of incorrect detection by the cameras due to environmental disturbance, e.g. light conditions (Figure 5c-iii). (3) To lengthen the probe delivery into a longer tube, a gear-chain-based delivery mechanism is superior. (4) In addition, to make the whole system more compact and easier for maintenance, a microcomputer with programmable I/O circuitry can be tested to manage all subsystems. (5) To increase the robustness of the trained CNN models, more and diversified data from the tubes with various types of defects are desired.

5 | CONCLUSION

In this study, we demonstrate an autonomous robot for STHE inspection. The robot effectively reduces human induced error in instrument manipulation and data analysis. To the best of our knowledge, this is the first autonomous robot that can operate ECT instrument for STHE inspection. This demonstration offers a new promise for improving power plant maintenance. In future, integration of different types of testing and analysis equipment would make

the robot more powerful or multifunctional for performing different tasks, which would require more sophisticated and task-specific mechanical systems, and accurate sensing and control systems.

ACKNOWLEDGEMENT

This material is based upon work supported by the Department of Energy (Award Number: DE-FE0031645).

CONFLICT OF INTERESTS

The authors declare no conflicts of interest.

DATA AVAILABILITY STATEMENT

Research data are not shared.

ORCID

Bujingda Zheng https://orcid.org/0000-0002-1099-3398
Yunchao Xie https://orcid.org/0000-0001-6216-1211
Jian Lin https://orcid.org/0000-0002-4675-2529

REFERENCES

Arad, B., Balendonck, J., Barth, R., Ben-Shahar, O., Edan, Y., Hellström, T. et al. (2020) Development of a sweet pepper harvesting robot. *Journal of Field Robotics*, *37*(6), 1027–1039.

Birrell, S., Hughes, J., Cai, J.Y. & Iida, F. (2020) A field-tested robotic harvesting system for iceberg lettuce. *Journal of Field Robotics*, *37*(2), 225–245.

Bolien, M. (2018) *Hybrid testing of an aerial refuelling drogue*. University of Bath.

Chang, F.-S., Hwang, L.-T., Liu, C.-F., Wang, W.-S., Lee, J.-N., Wang, S.-M. et al. (2015) Design of a pipeline inspection robot with belt driven ridged cone shaped skate model. *2015 IEEE International Conference on Robotics and Biomimetics (ROBIO)*, pp. 787–792.

Cherian, A., Morellas, V. & Papanikolopoulos, N. (2009) Accurate 3D ground plane estimation from a single image. In: *2009 IEEE International Conference on Robotics and Automation*, pp. 2243–2249.

Deng, W., Bao, J. & Ye, B. (2020) Defect image recognition and classification for eddy current testing of titanium plate based on convolutional neural network. *Complexity*, *2020*, 8868190–16479.

Djuric, A.M., Urbanic, R. & Rickli, J. (2016) A framework for collaborative robot (CoBot) integration in advanced manufacturing systems. *SAE International Journal of Materials and Manufacturing*, *9*(2), 457–464.

Engelberger, J.F. (2012) *Robotics in practice: management and applications of industrial robots*. Springer Science & Business Media.

Fischer, W., Caprari, G., Siegwart, R. & Moser, R. (2009). Compact magnetic wheeled robot for inspecting complex shaped structures in generator housings and similar environments. In: *2009 IEEE/RSJ International Conference on Intelligent Robots and Systems*, pp. 4116–4121.

García-Martín, J., Gómez-Gil, J. & Vázquez-Sánchez, E. (2011) Non-destructive techniques based on eddy current testing. *Sensors*, *11*(3), 2525–2565.

Gritsevskyi, A. (2016). Outlook for Global Nuclear Power: Energy, Electricity and Nuclear Power Estimates for the Period up to 2050. In: *Book of Abstracts of 11th International Conference of the Croatian Nuclear Society*, 120.

Hayashi, S., Yamamoto, S., Saito, S., Ochiai, Y., Kamata, J., Kurita, M. et al. (2014) Field operation of a movable strawberry-harvesting robot using a travel platform. *Japan Agricultural Research Quarterly: JARQ*, *48*(3), 307–316.

Ilon, B.E. (1975). Wheels for a course stable selfpropelling vehicle movable in any desired direction on the ground or some other base. In: Google Patents.

Kwon, Y.-S., Lee, B., Whang, I.-C. & Yi, B.-J. (2010) A pipeline inspection robot with a linkage type mechanical clutch. In: *2010 IEEE/RSJ International Conference on Intelligent Robots and Systems*, pp. 2850–2855.

Kwon, Y.-S. & Yi, B.-J. (2012) Design and motion planning of a two-module collaborative indoor pipeline inspection robot. *IEEE Transactions on Robotics*, *28*(3), 681–696.

Melani, A.H., Murad, C.A., Caminada Netto, A., Souza, G.F. & Nabeta, S.I. (2019) Maintenance strategy optimization of a coal-fired power plant cooling tower through generalized stochastic Petri nets. *Energies*, *12*(10), 1951.

Miao, R., Gao, Y., Ge, L., Jiang, Z. & Zhang, J. (2019) Online defect recognition of narrow overlap weld based on two-stage recognition model combining continuous wavelet transform and convolutional neural network. *Computers in Industry*, *112*, 103115.

Olson, E. (2011). AprilTag: A robust and flexible visual fiducial system. In: *2011 IEEE International Conference on Robotics and Automation*, pp. 3400–3407.

Park, J., Han, S.-J., Munir, N., Yeom, Y.-T., Song, S.-J., Kim, H.-J. et al. (2019) MRPC eddy current flaw classification in tubes using deep neural networks. *Nuclear Engineering and Technology*, *51*(7), 1784–1790.

Qu, Y., Durdevic, P. & Yang, Z. (2018) Smart-spider: Autonomous self-driven in-line robot for versatile pipeline inspection. *Ifac-papersonline*, *51*(8), 251–256.

Richardson, D.C. (2014) *Plant equipment and maintenance engineering handbook*. McGraw-Hill Education. Available at: http://accessengineeringlibrary.com/browse/plant-equipment-and-maintenance-engineering-handbook

Sadek, H. (2006) NDE technologies for the examination of heat exchangers and boiler tubes-principles, advantages and limitations. *Insight-Wigston then Northampton-*, *48*(3), 181–184.

Schoeneich, P., Rochat, F., Nguyen, O.T.-D., Caprari, G., Moser, R., Bleuler, H. et al. (2010). Tubulo—A train-like miniature inspection climbing robot for ferromagnetic tubes. In: *2010 1st International Conference on Applied Robotics for the Power Industry*, pp. 1–5.

Se, S. & Brady, M. (2002) Ground plane estimation, error analysis and applications. *Robotics and Autonomous Systems*, *39*(2), 59–71.

Shorten, C. & Khoshgoftaar, T.M. (2019) A survey on image data augmentation for deep learning. *Journal of Big Data*, *6*(1), 1–48.

Smith, R. (2005) *Chemical process: design and integration*. John Wiley & Sons.

Speight, J.G. (2021) *Coal-fired power generation handbook*. John Wiley & Sons.

Taheri, H., Qiao, B. & Ghaeminezhad, N. (2015) Kinematic model of a four mecanum wheeled mobile robot. *International Journal of Computer Applications*, *113*(3), 6–9.

T.E.M.Association. (1952) Standard of tubular exchanger manufacturers association. The association.

Udpa, L., Ramuhalli, P., Benson, J. & Udpa, S. (2004). Automated analysis of eddy current signals in steam generator tube inspection. In: *Proceedings of the 16th WCNDT*.

Wang, H., Xie, Y., Li, D., Deng, H., Zhao, Y., Xin, M. et al. (2020) Rapid identification of X-ray diffraction patterns based on very limited data by interpretable convolutional neural networks. *Journal of Chemical Information and Modeling*, *60*(4), 2004–2011.

Wang, J. & Olson, E. (2016). AprilTag 2: Efficient and robust fiducial detection. In: *2016 IEEE/RSJ International Conference on Intelligent Robots and Systems (IROS)*, 4193–4198.

Williams, H., Ting, C., Nejati, M., Jones, M.H., Penhall, N., Lim, J. et al. (2020) Improvements to and large-scale evaluation of a robotic kiwifruit harvester. *Journal of Field Robotics*, *37*(2), 187–201.

Xiong, Y., Ge, Y., Grimstad, L. & From, P.J. (2020) An autonomous strawberry-harvesting robot: design, development, integration, and field evaluation. *Journal of Field Robotics*, *37*(2), 202–224.

Xiong, Y., Peng, C., Grimstad, L., From, P.J. & Isler, V. (2019) Development and field evaluation of a strawberry harvesting robot with a cable-driven gripper. *Computers and Electronics in Agriculture*, *157*, 392–402.

Yamamoto, S., Hayashi, S., Yoshida, H. & Kobayashi, K. (2014) Development of a stationary robotic strawberry harvester with a picking mechanism that approaches the target fruit from below. *Japan Agricultural Research Quarterly: JARQ*, *48*(3), 261–269.

Zhu, P., Cheng, Y., Banerjee, P., Tamburrino, A. & Deng, Y. (2019) A novel machine learning model for eddy current testing with uncertainty. *NDT & E International*, *101*, 104–112.

SUPPORTING INFORMATION

Additional supporting information can be found online in the Supporting Information section at the end of this article.

How to cite this article: Zheng, B., Su, J.-W., Xie, Y., Miles, J., Wang, H., Gao, W., et al. (2022) An autonomous robot for shell and tube heat exchanger inspection. *Journal of Field Robotics*, 39, 1165–1177. https://doi.org/10.1002/rob.22102